AIP | Physics of Fluids

Vortex dynamics of in-line twin synthetic jets in a laminar boundary layer

Xin Wen, Hui Tang, and Fei Duan

Citation: Physics of Fluids **27**, 083601 (2015); doi: 10.1063/1.4928216
View online: http://dx.doi.org/10.1063/1.4928216
View Table of Contents: http://scitation.aip.org/content/aip/journal/pof2/27/8?ver=pdfcov
Published by the AIP Publishing

PHYSICS OF FLUIDS **27**, 083601 (2015)

Vortex dynamics of in-line twin synthetic jets in a laminar boundary layer

Xin Wen,[1] Hui Tang,[2,a)] and Fei Duan[1]
[1]*School of Mechanical and Aerospace Engineering, Nanyang Technological University, Singapore 639798, Singapore*
[2]*Department of Mechanical Engineering, The Hong Kong Polytechnic University, Kowloon, Hong Kong, China*

(Received 27 December 2014; accepted 27 July 2015; published online 13 August 2015)

An experimental investigation is conducted on the vortices induced by twin synthetic jets (SJs) in line with a laminar boundary layer flow over a flat plate. The twin SJs operating at four different phase differences, i.e., $\Delta\phi = 0°$, 90°, 180°, and 270°, are visualized using a stereoscopic color dye visualization system and measured using a two-dimensional particle image velocimetry (PIV) system. It is found that depending on the phase difference of twin SJs, three types of vortex structures are produced. At $\Delta\phi = 90°$, the two hairpin vortices interact in a very constructive way in terms of the vortex size, strength, and celerity, forming *one combined vortex*. At $\Delta\phi = 270°$, the two individual hairpin vortices do not have much interaction, forming *two completely separated hairpin vortices* that behave like doubling the frequency of the single SJ case. At $\Delta\phi = 0°$ and 180°, the two hairpin vortices produced by the twin SJ actuators are close enough, with the head of one hairpin vortex coupled with the legs of the other, forming *partially interacting vortex structures*. Quantitative analysis of the twin SJs is conducted, including the time histories of vortex circulation in the mid-span plane as well as a selected spanwise-wall-normal plane, and the influence of the twin SJs on the boundary layer flow filed. In addition, dynamic mode decomposition analysis of the PIV data is conducted to extract representative coherent structures. Through this study, a better understanding in the vortex dynamics associated with the interaction of in-line twin SJs in laminar boundary layers is achieved, which provides useful information for future SJ-array applications. © *2015 AIP Publishing LLC*. [http://dx.doi.org/10.1063/1.4928216]

I. INTRODUCTION

Synthetic jet (SJ), also known as a zero-net-mass-flux jet, provides a novel means of flow control due to its ability of injecting non-zero momentum into external flow with zero net mass flux.[1–6] A typical SJ actuator (SJA) consists of a cavity with an oscillatory diaphragm on its bottom side and an orifice on the opposite. The diaphragm's periodic downward and upward motions generate a succession of vortex rings/pairs that propagate away from the orifice/slot, synthesizing a SJ.

When a SJ is deployed in a boundary layer flow, the streamwise vortices induced by the interaction of the SJ with the crossflow are capable of energizing the boundary layer flow to delay flow separation.[7,8] Studies have shown that these vortex structures vary from hairpin vortices, stretched vortex rings, to tilted vortex rings depending on the jet-to-free stream velocity ratio and dimensionless stroke length.[9,10] It was further found that the hairpin vortices and stretched vortex rings are more capable of flow separation delay.[11,12]

Although in many flow control applications SJs are deployed in arrays, the detailed interaction among these SJs in boundary layers, especially the resulting vortex structures, has not been well studied and understood to the extent similar to that for single SJs. Only very limited literature in

---

[a)] Author to whom correspondence should be addressed. Electronic mail: h.tang@polyu.edu.hk this aspect was reported. Watson *et al.*[13] examined the interaction between two neighboring SJs at various yaw angles relative to a boundary layer flow using surface flow visualization and found twin SJs of in-line configuration can interact in a constructive way to generate larger paint pattern. They hypothesized that under this condition these two SJs are combined to form a stronger vortex structure. Liddle *et al.*[14,15] investigated the effect of relative phase difference between the in-line twin SJs in a boundary layer using hot-wire measurements. The power spectral density (PSD) analysis of near-wall velocity in the mid-span plane reveals that the frequency corresponding to the major spectral peak coincides with the SJ operating frequency in most of the investigated cases, but at phase difference $\Delta\phi = 270°$, the peak occurs at a frequency twice of the actuation frequency. Recently Iai *et al.*[16] and Honami and Motosuke[17] did more comprehensive investigations on in-line twin SJs in a channel flow using particle image velocimetry (PIV) measurements. They found the vortex structure produced by the downstream SJ is strongly affected by the upstream SJ, and the vortex structure produced by the upstream SJ is able to maintain more coherence. Although encouraging, their vortex structures visualized using vorticity iso-surfaces and velocity vector fields are not well represented due to low quality images. In addition, in their results it is hard to differentiate the contribution of individual SJs to the resulting vortex structures due to the same color used for the iso-surfaces, making the in-depth analysis challenging.

Aiming to uncover more flow physics associated with SJ arrays, the present study is focused on the vortex dynamics of in-line twin SJs at different phase differences in a laminar boundary layer. A water tunnel experiment is conducted to facilitate this study, in which stereoscopic color dye visualization is used to show complex interacting flow structures, and PIV measurements are conducted to provide quantitative data about the interaction. To make the analysis more focused, some parameters, such as the yaw angle, distance between the two SJAs, and strength of the two SJs, are fixed.

II. METHODOLOGY

A. Test rig

The present experimental investigation is conducted in a low-speed water tunnel with a test section of 1 m (L) × 0.45 m (W) × 0.45 m (H). A laminar boundary layer flow is generated along a long test plate parallel to the water flow. Fig. 1(a) shows a sketch of the test plate, which consists of two pieces of 10 mm thick and 430 mm wide flat plates, the upstream one 600 mm long and the downstream one 150 mm long. These two flat plates are joined together using hinges, such that the angle between them is adjustable. Since in the present study the focus is only on the interaction of twin SJs in a flat-plate laminar boundary layer, this angle is fixed at 180° to simply extend the total length of the test plate to 750 mm. A 1:5 elliptical leading edge is manufactured on the test plate to prevent possible flow separation.

As shown in the side view of Fig. 1(a), two SJAs are mounted on the test plate, with their cavities located on the upper surface of the test plate and their orifices flush to the lower surface.

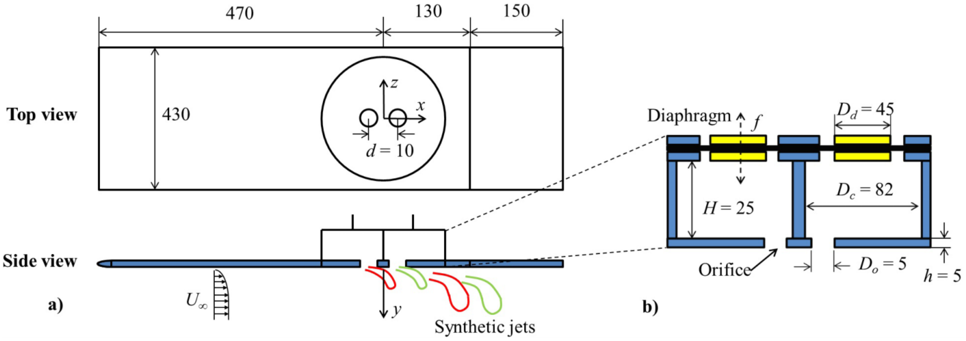

FIG. 1. Schematic of (a) the test plate and (b) the twin SJAs (not to scale, all dimensions in mm).

As shown in the close view in Fig. 1(b), each SJA has a cylindrical cavity with an orifice plate at its bottom side and a moving diaphragm clamped to its top side. The cavity has a diameter of $D_c = 82$ mm and a height of $H = 25$ mm, and the orifice has a diameter of $D_o = 5$ mm and depth of $h = 5$ mm. In the present study, the orifices of the two SJAs are not placed at the center of their respective orifice plates. Instead, they are placed close to each other, with the center-to-center distance fixed at $d = 10$ mm, i.e., $d/D_o = 2$. This off-center design may cause slight asymmetry of vortex rings produced from the SJAs. However, this asymmetry can be overcome by introducing a relatively stronger crossflow, which, although not presented here, has been confirmed in a control test that compares the vortex structures issued from each individual SJA in a boundary layer. In addition, as indicated in Fig. 1(a), the centers of these two orifices are aligned with the crossflow direction, and their midpoint is 470 mm away from the test plate's leading edge. As depicted in Fig. 1(a), the origin of the coordinate system used in the present study is set at this midpoint, with the x axis pointing to the crossflow flow direction, y axis pointing to downward wall-normal direction, and z axis pointing to the spanwise direction.

The diaphragm of the SJA is made of a thin rubber sheet sandwiched by two metal plates of diameter $D_d = 45$ mm, whose center is attached to a permanent magnetic shaker (LDS V201 from Brüel and Kjær) via a steel rod. A 2.5 mm gap between the moving metal plates and their surrounding base plates ensures a piston-like motion of the diaphragm. When in operation, the diaphragm oscillates in a sinusoidal manner with tunable peak-to-peak displacement Δ and frequency f. If the working fluid is incompressible as in the present study, the time-averaged jet velocity $\bar{U}_o$ over an entire actuation cycle T can be estimated in terms of Δ and f,

$$\overline{U}_o = \frac{1}{T}\int_0^{T/2} u_o(t)dt = \Delta f(\frac{D_d}{D_o})^2, \tag{1}$$

where $u_o(t)$ is the instantaneous jet velocity.

If both the SJAs are in operation, the oscillation amplitude and frequency of their diaphragms are controlled by two synchronized sine wave signals using LabVIEW. The operational phase difference between these two SJAs can be tuned with a resolution of 1°. To read the oscillation amplitude, the motion of the diaphragm center is measured using an eddy current displacement sensor (ECL202 from Lion Precision).

B. Selection of test case

Based on dimensional analysis, the behavior of a single SJ in quiescent conditions can be characterized by the dimensionless stroke length L and Reynolds number Re_L. L is defined as

$$L = \frac{L_o}{D_o} = \frac{\overline{U}_o}{fD_o}, \tag{2}$$

where L_o is the stroke length representing the length of the fluid column expelled during the SJ blowing stroke, and $\overline{U}_o$ is the time-averaged blowing velocity over an entire actuation cycle. The stroke length based Reynolds number, Re_L, is the ratio of inertial forces to viscous forces,

$$Re_L = \frac{\overline{U}_o L_o}{\nu}, \tag{3}$$

where ν is the fluid kinematic viscosity. Re_L characterizes the SJ vortex circulation and hence is a useful indicator of SJ vortex strength. Tang and Zhong[18] gave an estimation of the non-dimensional total circulation, or vorticity flux produced across the SJA orifice exit during one actuation cycle in quiescent conditions,

$$\frac{\Gamma}{U_\infty D_o} \approx (\frac{\pi^2}{8})(\frac{\nu}{U_\infty D_o})Re_L. \tag{4}$$

When a crossflow is involved, the velocity ratio VR quantifies the ratio of the SJ velocity to the crossflow velocity U_∞,

$$VR = \frac{\overline{U_o}}{U_\infty}, \tag{5}$$

VR determines the orientation angle between the emerging SJ vortex structures and the flat plate. It also affects the trajectory of SJs when they propagate downstream in the crossflow: as VR increases, the trajectory moves away from the plate. At different L and VR values, Jabbal and Zhong[19] identified three types of vortex structures that are induced by a single SJ issued into a laminar boundary layer, i.e., hairpin vortices, stretched vortex rings, and tilted vortex rings. Among these structures, hairpin vortices are closest to the wall and hence are more capable of delaying flow separation. They further revealed that hairpin vortices can be induced in the range of $1.5 < L < 3.5$ and $0.1 < VR < 0.3$.

If two identical SJAs are placed in the crossflow and operated with the same jet velocities and frequencies, three more non-dimensional parameters are required to describe the resulting flow: the non-dimensional center-to-center distance between the two SJA orifices, d/D_o, the angle between the crossflow direction and the line connecting the two orifice centers, ψ, and the operational phase difference between the two SJAs, $\Delta\phi$.

The above analysis indicates six independent non-dimensional parameters that characterize the behavior of twin SJs in crossflows, i.e., L, Re_L, VR, d/D_o, ψ, and $\Delta\phi$. To make the present study more focused, a case is selected such that the two identical SJAs are arranged in line ($\psi = 0$) and with a fixed distance $d/D_o = 2$. To ensure the production of hairpin vortices, the crossflow velocity is kept at $U_\infty = 0.11$ m/s, and the diaphragm peak-to-peak displacement and oscillating frequency are set at $\Delta = 0.105$ mm and $f = 2$ Hz, respectively, for both SJAs. From Eqs. (1), (2), and (5), these settings yield $L = 1.7$ and $VR = 0.15$, which fall in the region of hairpin vortex production suggested by Jabbal and Zhong.[19] In addition, the total circulation or vorticity flux produced across the SJA orifice exit in quiescent conditions is estimated as $\Gamma/U_\infty D_o = 0.32$ using Eqs. (3) and (4).

C. PIV

To facilitate the PIV measurements, the entire water tunnel is seeded with Dantec Dynamics polyamide seeding particles with a mean diameter of 20 μm and density of 1030 kg/m^3. According to the Stokes' drag law, the settling velocity of these particles is about 7 μm/s, much slower than the crossflow speed. This suggests that the seeding particles are capable of following the flow quite accurately.[20,21]

The PIV measurements are conducted in the mid-span plane, which bisects the twin SJAs, as well as in a selected spanwise-wall-normal plane, i.e., $x = 8D_o$, as shown in Fig. 2(a). A laser sheet of approximately 1 mm thickness is generated by a 200 mJ double pulsed Nd:YAG laser generator to illuminate the seeding particles. A FlowSense 2M CCD camera with a Nikon 105 mm lens is used to capture a field of view of $x = -4 \sim 11D_o$ and $y = 0D_o \sim 5D_o$ in the mid-span plane. The resulting velocity vectors are resolved using a two-frame cross-correlation algorithm, in which a 32×32 pixel interrogation area (IA) with an overlap ratio of 50% was chosen, giving a 0.76 mm spatial resolution. The images in the spanwise-wall-normal plane are taken through a small window located at the first elbow downstream of the water tunnel's test section. In this plane, the field of

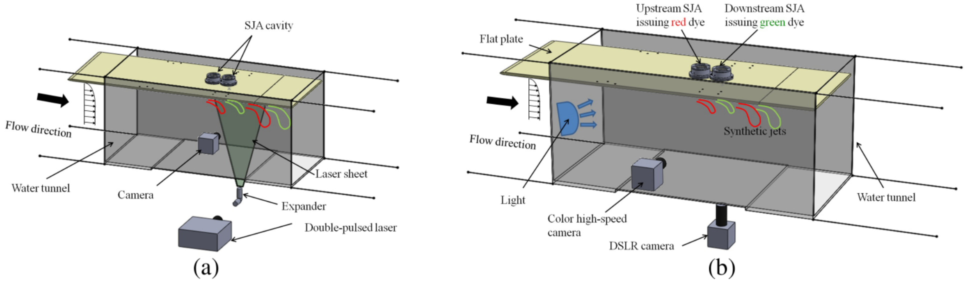

FIG. 2. Schematic of (a) the PIV measurement system and (b) the stereoscopic dye visualization system.

view is $y = 0 \sim 5D_o$ and $z = -4D_o \sim 4D_o$. Considering a large minimum-required distance between this plane and the camera due to the actual water tunnel dimensions, a smaller IA of 16 × 16 pixel is adopted in the two-frame cross-correlation algorithm, hence yielding a 0.51 mm spatial resolution. The selection of this IA has been proved adequate by comparing the resulting velocity fields obtained with a 32 × 32 pixel IA.

The mean velocity profile of the developed boundary layer flow without SJs is first obtained using 300 consecutive PIV images taken at a frequency of 10 Hz in the mid-span plane. According to the boundary layer theory, given the crossflow velocity of $U_\infty = 0.11$ m/s, a laminar boundary layer developed along the test plate shall have a thickness of about 10 mm and a momentum thickness based Reynolds number of about $Re_\theta = 150$ at the origin of the current coordinate system. As shown in Fig. 3(a), the measured mean velocity profile in the boundary layer agrees with the Blasius solution very well, confirming the zero-pressure-gradient laminar nature of the current boundary layer. In addition, the measured profile of root-mean-square streamwise velocity fluctuation u' is presented in Fig. 3(b), which shows that the fluctuation is less than 1% in the free stream and less than 2.5% in the boundary layer. The slightly higher-level fluctuation in the near-wall region may be caused by the existence of the two open SJA orifices located slightly upstream.

When the SJs are introduced, a LabVIEW virtual instrument is used to generate synchronized sinusoidal waveforms for the SJA diaphragms and transistor-transistor logic (TTL) signals for the PIV timing controller, respectively, with which the laser is controlled to shoot at selected phases. Herein, the phase is defined by the diaphragm movement of the upstream SJA: $t/T = 0$ (and 1), 1/4, 1/2, and 3/4 correspond to the beginning of blowing, maximum blowing, beginning of ingestion, and maximum ingestion, respectively, where T is the SJA operation period. To better present the results, velocity vector images at eight equispaced phases, i.e., $t/T = 0.075$, 0.2, 0.325, 0.45, 0.575, 0.7, 0.825, and 0.95, within one actuation cycle are obtained. At each phase, by following Jabbal and Zhong,[11] 60 vector images are used to calculate phase-averaged quantities. Although not shown here, a convergence study has also confirmed that this sample number is adequate for twin-SJ-induced flow structures in laminar boundary layers.

As the major uncertainty source, the root-mean-square fluctuation of the PIV measured particle displacement is estimated to be about 0.08 pixel in the field images.[22] Therefore, the measurement uncertainties determined from the recursive image interrogation procedure are approximately 1% in the streamwise and wall-normal velocity components where the particle displacement is about 8 pixels in the 32 × 32 pixel IA and 2% in the spanwise velocity component where the particle displacement is about 4 pixels in the 16 × 16 pixel IA. The vorticity was calculated using a standard central difference scheme, and its uncertainty e_ω was estimated from the uncertainty in velocity e_u using the formula $e_\omega = (u_{max} \cdot e_u/\Delta x)/\omega_{max}$, where Δx is the grid size, u_{max} the maximum velocity, and ω_{max} the maximum vorticity. With this formula, the uncertainty for the resulting vorticity is estimated to be up to 5.6% of the maximum vorticity in the field.

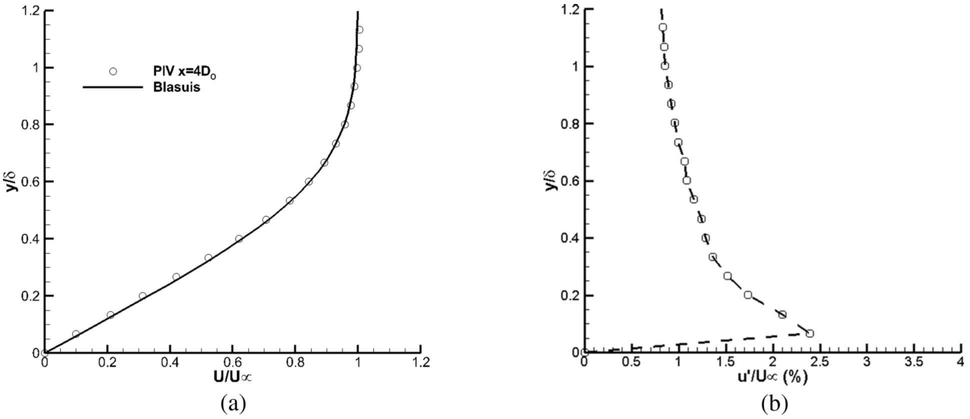

(a) (b)

FIG. 3. (a) Comparison of PIV-measured mean velocity profile and the Blasius solution at $x = 4D_o$ in the mid-span plane; (b) PIV-measured profile of root-mean-square streamwise velocity fluctuations at $x = 4D_o$ in the mid-span plane.

D. Stereoscopic color dye visualization system

To visualize and differentiate the twin SJs in the crossflow, food dye of two different colors is used to fill the SJAs. The upstream SJA is filled with red dye and the downstream SJA filled with green dye. The dye is premixed with methanol to achieve a density very close to the water's. To capture the dye patterns produced by the SJs, a color high-speed camera (MotionBLITZ EoSens) is used from the side of the water tunnel test section to form the side view, and a digital single-lens reflex (DSLR) camera (Canon EOS 60D) is used underneath the water tunnel to form the plan view. Both the cameras operate with the same frame rate of 60 fps, providing a quasi-three-dimensional dye visualization of the twin SJs as depicted in Fig. 2(b).

E. Quantitative analysis methods

With the velocity information obtained from the PIV measurements, the SJ-induced coherent structures are identified using local swirling strength, λ_{ci}, the imaginary part of the complex eigenvalue pair of local velocity gradient.[23] In the present study, an iso-value of $\lambda_{ci} = 0.25$ is used to determine the edge of vortex structures so as to show the shape of vortex structures while filtering out low λ_{ci} value noise. Vortex centers are then determined using local maximum λ_{ci} values.

In the 2D PIV data planes, the strength of identified vortex structures is quantified using vortex circulation $\mathit{\Gamma}$,

$$\mathit{\Gamma} = \int_{\Sigma} \omega \, \mathrm{d}A, \tag{6}$$

where $\sum$ is the identified vortex edge, ω the vorticity contained in the vortex, and A the area of the vortex.

In the present study, all the results showed are non-dimensional, with the length scale normalized using the SJA orifice diameter D_o, the time scale using the SJA operating period T, the velocity using the crossflow velocity U_∞, the vorticity using U_∞/D_o, and the vortex circulation using $U_\infty D_o$.

F. Dynamic mode decomposition (DMD) analysis method

The DMD analysis method is a useful tool for extracting coherent flow structures from unsteady flows. Different from another popular method—the proper orthogonal decomposition (POD) analysis method that extracts flow structures based on their energy ranking—DMD extracts flow structures based on their contributions to flow dynamics. That is, DMD is able to extract spatial modes based on their frequency content, which makes it a suitable method to analyze dynamics of a flow system involving multiple frequency components like in the present study.[24,25]

In DMD, a time sequence of flow field data is organized by a matrix

$$U_1^N = \{\boldsymbol{u}_1, \boldsymbol{u}_2, \cdots, \boldsymbol{u}_N\}, \tag{7}$$

where $\boldsymbol{u_i}$ is a vector representing a snapshot of the flow field at time t_i. If there is a linear mapping A connecting the snapshot $\boldsymbol{u_i}$ to its subsequent snapshot $\boldsymbol{u_{i+1}}$, the time sequence of the flow field data can be re-formulated as

$$U_1^N = \{\boldsymbol{u}_1, A\boldsymbol{u}_1, \cdots, A^{N-1}\boldsymbol{u}_1\}. \tag{8}$$

The goal of DMD is to extract the dynamic characteristics, i.e., eigenvalues and eigenvectors, of the dynamic process described by A based on the subsequence U_1^{N-1}. After the decomposition, DMD provides the following representation of a flow field $\boldsymbol{u}(\boldsymbol{x}, t)$:[26]

$$\boldsymbol{u}(\boldsymbol{x}, t) = \sum_{n=1}^{N} b_n \exp(\mu_n t) \boldsymbol{\Psi}_n(\boldsymbol{x}), \tag{9}$$

where b_n is the corresponding amplitude and μ_n is the corresponding frequency. $\boldsymbol{\Psi}_n$ is the nth DMD mode,

$$\boldsymbol{\Psi}_n(\boldsymbol{x}) = U_1^{N-1} \boldsymbol{X}_n, \tag{10}$$

where X_n is the nth eigenvector of A. The detailed procedures for determining the DMD modes are given in Schmid.[24,25]

In the present study, $N = 240$ is chosen and the analysis focus is only on up to the first four modes. Since there are 16 equispaced snapshots of flow field data per second, the present DMD analysis can only capture the flow dynamics up to 8 Hz, four times of the SJ actuation frequency (2 Hz).

III. SINGLE SJs IN A LAMINAR BOUNDARY LAYER

Before the interaction of the twin SJs is investigated, the flow pattern of a single SJ in the laminar boundary layer is presented as a baseline case. As expected, a sequence of hairpin vortices is generated from the upstream SJA under the present test conditions, with a clear hairpin head followed by a pair of legs in the boundary layer as shown in Fig. 4(a). The formation of these hairpin vortices is a direct result of the SJ-boundary-layer interaction.[27] The well-defined vortex tubes captured in the dye visualization indicate the laminar nature of the coherent structures.

PIV measurements also captured the hairpin vortices. In the mid-span plane as shown in Fig. 4(b), a hairpin vortex is well captured by an inverted-hook-shaped, positive wall-normal velocity region that follows a smaller negative wall-normal velocity region. The streamwise gap between these two regions at about $x = 5D_o$ defines the hairpin head, and the slant near-wall portion of the positive velocity region represents the upwash flow region between the two hairpin legs. The hairpin

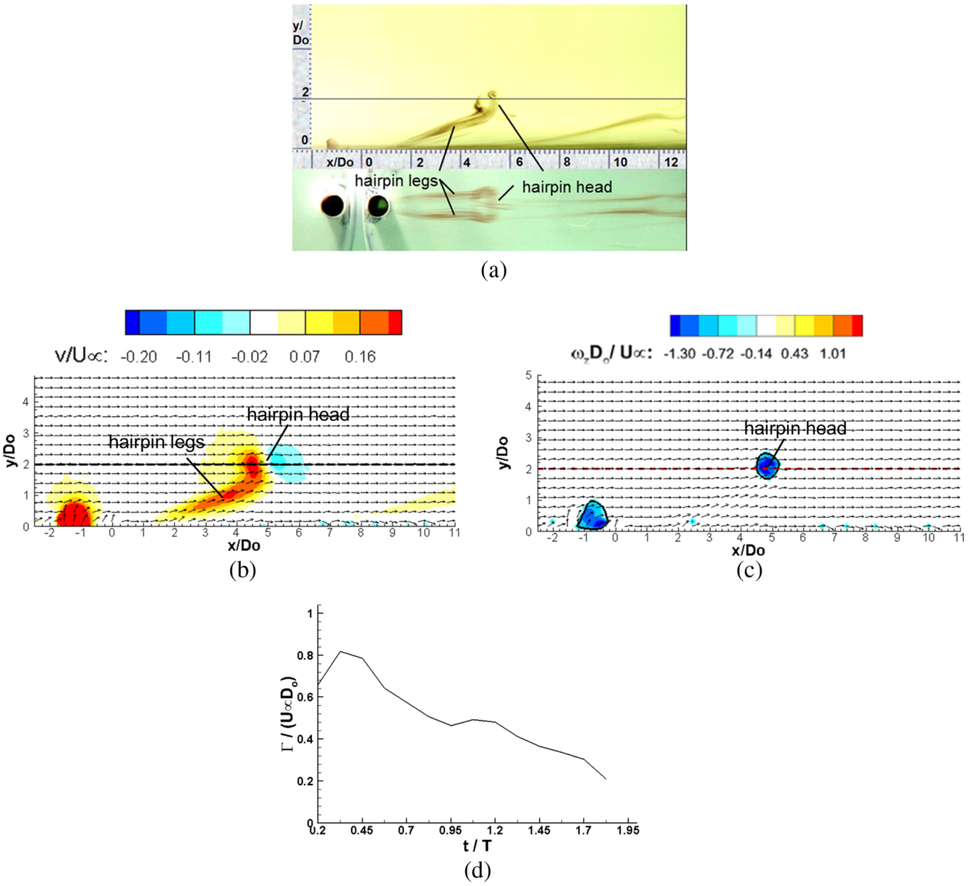

(a)

(b)

(c)

(d)

FIG. 4. (a) Stereoscopic dye images of a single SJ in a laminar boundary layer. The line in the side view indicates the edge of the boundary layer. (b) Contour of wall-normal velocity superimposed by velocity vectors and (c) hairpin head captured by $\lambda_{ci} = 0.25$ and contour of spanwise vorticity in the mid-span plane at $t/T = 0.2$. (d) Time history of hairpin vortex circulation.

head is also captured by an enclosed area identified with an iso-value of $\lambda_{ci} = 0.25$, as shown in Fig. 4(c). With this enclosed area, the circulation around the hairpin head can be evaluated using Eq. (6). Fig. 4(d) plots a time history of non-dimensional circulation $\Gamma/U_\infty D_o$ around the hairpin head. This curve indicates that $\Gamma/U_\infty D_o$ grows in the beginning, achieves its maximum value at about $t/T = 0.45$ that is near the end of blowing stroke, and then gradually decreases under the influence of dramatic turning and stretching of the hairpin vortex in the boundary layer. Its peak value is $\Gamma/U_\infty D_o \approx 0.82$, which is about 2.6 times of the analytical value $\Gamma/U_\infty D_o = 0.32$ estimated by Eqs. (3) and (4). The significantly larger value obtained from the PIV data is likely caused by two main reasons: First, since the analytical value estimated in Eq. (3) is based on a uniform (or top-hat) jet velocity profile assumption, non-uniformity of the actual velocity profile will result in greater circulation values. Second, the analytical value 0.32 estimated in Eq. (3) is for vortices just coming out of the SJA orifice, while the value 0.82 is the peak value that develops for a while and carries additional circulation entrained during the vortex development.

IV. IN-LINE TWIN SJs IN A LAMINAR BOUNDARY LAYER

A. Behavior of in-line twin SJs at various phase differences

By controlling the phase difference between the two SJAs, the interaction of the in-line twin SJs is investigated in the same laminar boundary layer. Here, the phase difference is defined as $\Delta\phi = \phi_u - \phi_d$, where ϕ_u and ϕ_d are the phases of the upstream SJA and of downstream SJA, respectively. Four different phase differences are investigated, i.e., $\Delta\phi = 0°,\ 90°,\ 180°$, and $270°$ (or $-90°$). The dye visualization results are shown in Fig. 5, in which the flow structures in red are produced from the upstream SJA and those in green are produced from the downstream SJA. The corresponding contours of wall-normal velocity superimposed by velocity vectors are presented in Fig. 6, which are obtained from the PIV measurements. It can be seen that the flow structures captured by the PIV measurements generally match with the structures in the dye visualization in terms of the vortex size and shape.

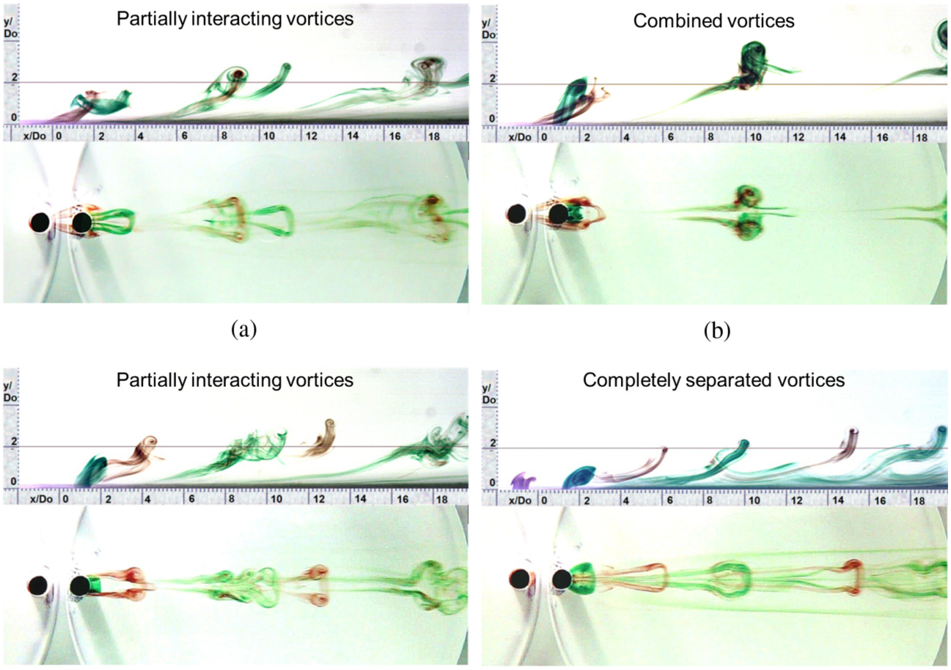

(a) (b) (c) (d)

FIG. 5. Stereoscopic dye images of the twin SJs at various phase differences (a) $\Delta\phi = 0°$, (b) $\Delta\phi = 90°$, (c) $\Delta\phi = 180°$, (d) $\Delta\phi = 270°$.

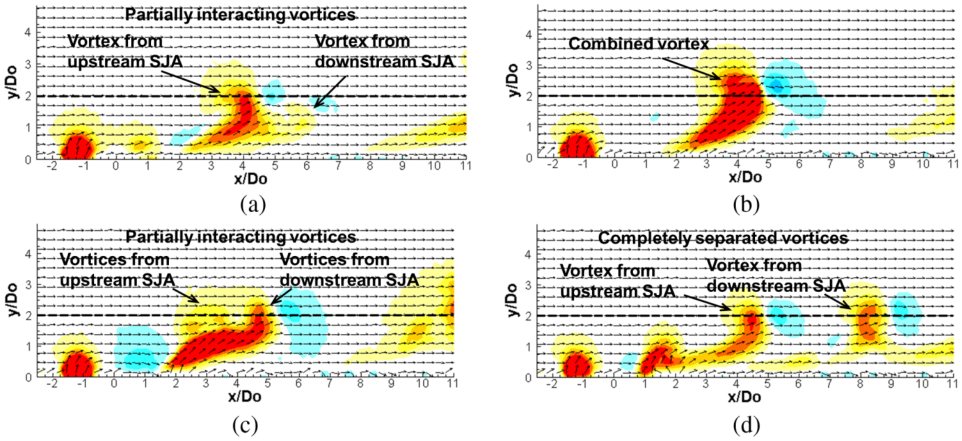

(a) (b) (c) (d)

FIG. 6. Contour of wall-normal velocity and velocity vectors at various phase differences at $t/T = 0.2$. (a) $\Delta\phi = 0°$, (b) $\Delta\phi = 90°$, (c) $\Delta\phi = 180°$, (d) $\Delta\phi = 270°$. Refer to Fig. 4(b) for the color map.

Three different types of flow structures are observed, i.e., one combined vortex at $\Delta\phi = 90°$, two completely separated hairpin vortices at $\Delta\phi = 270°$, and partially interacting flow structures at $\Delta\phi = 0°$ and 180°. At $\Delta\phi = 90°$, the hairpin vortex produced by the downstream SJA emerges when its counterpart from the upstream SJA just passes by. As shown in Fig. 5(b), these two hairpin vortices perfectly merge together, forming a new vortex structure with a larger head and more strength. The new vortex structure penetrates the boundary layer much faster than the single SJ (Fig. 4(a)). The PIV measurements also capture the merging of the two hairpin vortices. In Fig. 6(b), the size of a single inverted-hook-shaped contour region and its accompanying negative wall-normal velocity region is significantly larger than that in the single SJ case (Fig. 4(b)), confirming the increased strength of the combined vortex. Hence at this phase difference, the two hairpin vortices interact in a very constructive way in terms of the vortex size, strength, and celerity.

At $\Delta\phi = 270°$, as the hairpin vortex produced by the downstream SJA appears, its counterpart from the upstream SJA has already passed the downstream SJA for about half an actuation cycle, i.e., $T/2$. As such, the newly emerging hairpin vortex is not affected too much. As shown in Fig. 5(d), the resulting flow structures are then a sequence of hairpin vortices with the same color appearing in an alternate manner. It seems like doubling the frequency of the single SJ. From this dye visualization, an interesting phenomenon is observed that the tip of each hairpin leg is lifted up and entrained by its following hairpin vortex, resulting in a wave-like flow pattern in the near-wall region. The PIV measurements also capture these two completely separated hairpin vortices as shown in Fig. 6(d). The contour size further reveals that the hairpin vortex issued from the downstream SJA is weaker than its counterpart issued from the upstream SJA.

At $\Delta\phi = 0°$ and 180°, the two hairpin vortices produced by the twin SJAs are close, with the head of one hairpin vortex coupled with the legs of the other, forming complex vortex structures as shown in Figs. 5(a) and 5(c). The time difference between these two hairpin vortices is about a quarter of an actuation cycle, i.e., $\pm T/4$. As shown in Fig. 5(a), at $\Delta\phi = 0°$ the strong upwash flow induced between the two legs of the trailing hairpin vortex (in red) lifts up the mid-portion of the leading hairpin legs (in green), part of which is even entrained into the head of the trailing hairpin vortex making it continue growing its size.

The story changes at $\Delta\phi = 180°$. As shown in Fig. 5(c), the interaction of the trailing hairpin head (in green) with the leading hairpin legs (in red) results in the trailing hairpin head breaking up into multiple smaller "vortex heads." This is because that during its formation process the hairpin vortex issued from the downstream SJA is significantly disturbed by its counterpart and hence has no time to fully develop its own coherence. By such intense disturbance, the flow pattern of the trailing hairpin vortex is not perfectly laminar but a little bit turbulent. In addition, by comparing Figs. 5(a) and 5(c), the leading hairpin vortex issued from the upstream SJA at $\Delta\phi = 180°$ seems more sustained than the leading hairpin vortex issued from the downstream SJA at $\Delta\phi = 0°$. These features are also well captured by the PIV measurements. As shown in Figs. 6(a) and 6(c), at $\Delta\phi = 0°$, the trailing hairpin vortex is much stronger than the leading hairpin vortex, whereas at $\Delta\phi = 180°$, the trailing hairpin vortex merges into the legs of the leading hairpin vortex, forming a larger combined vortex structure. On top of this combined vortex structure lie two weak vortex heads, which are consistent to what has been observed in the dye visualization as shown in Fig. 5(c).

With the PIV data, the evolution of spanwise vortex circulation carried by hairpin heads can be evaluated and compared as shown in Fig. 7(a). At $\Delta\phi = 90°$, in its initial developing phase, the hairpin vortex issued from the upstream SJA shares a strength evolution process similar to that in the single SJ case. After the vortex meets and merges with its counterpart, the circulation of combined vortex continues increasing and reaches a peak value $\Gamma/U_\infty D_o = 1.15$ at $t/T = 0.7$, which is a 40% increment compared to the peak value in the single SJ case. Similar to that in single hairpin vortices, after the peak, a plateau appears between $t/T = 1.2$ and 1.7. At $\Delta\phi = 270°$, with the weakest interaction, it is not surprising to see that the hairpin vortex from the upstream SJA shares very similar circulation evolution process to that in the single SJ case, except that it has a slightly larger peak value, which is likely caused by the downwash flow induced through the suction of the downstream SJA when the vortex passes by. Since in this case the hairpin vortex issued from the downstream SJA emerges 270° later (or 90° earlier), its circulation evolution curve is shifted to the left by about $0.25T$. Due to the disturbance of its preceding vortex issued in the previous cycle during its emerging process, this hairpin vortex has a significant lower circulation peak value ($\Gamma/U_\infty D_o = 0.65$) compared to that of its counterpart ($\Gamma/U_\infty D_o = 0.90$) as well as of the single hairpin vortex ($\Gamma/U_\infty D_o = 0.82$). Interestingly, its strength increases again after a gradual decrease (see the black symbolled line). This rebound is caused by the absorption of its preceding hairpin legs, a phenomenon clearly shown in the dye visualization as in Fig. 5(d).

The evolution of streamwise vortex circulation in a spanwise-wall-normal plane $x = 8D_o$ is also compared as shown Fig. 7(b). To obtain this plot, the circulation of primary streamwise vortices in that plane is calculated at the eight evenly distributed instants during one actuation cycle. In this way, the vortex strength at different portions of the interacting vortex structure is presented and compared. As expected, the variation of vortex circulation at $\Delta\phi = 90°$ shares a trend similar to that in the single SJ case and shows the highest peak at the instant when the vortex head passes the plane. Oppositely, at $\Delta\phi = 270°$, two peaks of lower-amplitude circulation appear, confirming the passage of two separated hairpin vortices.

In the same plane, i.e., $x = 8D_o$, time-averaged streamwise vorticity contours superimposed by velocity vectors are shown in Fig. 8. The counter-rotating hairpin legs and their associated secondary vortices are well captured, which are represented by pairs of streamwise vorticity concentration areas that are symmetric about the mid-span plane. Compared to the single SJ, the twin SJs regardless of their phase difference are able to produce either stronger or larger primary and secondary vortices. Among the four twin-SJ cases, the primary vortices reach farthest from the

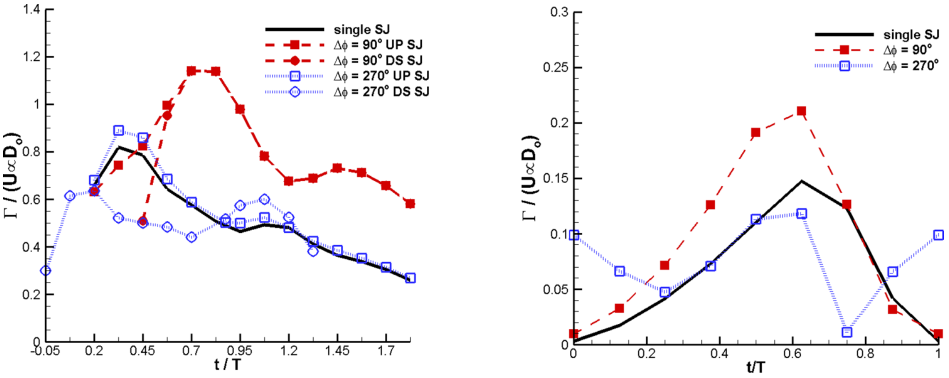

(a) (b)

FIG. 7. Time histories of vortex circulation of single hairpin vortex and interacting structures with $\Delta\phi = 90°$ and 270° (a) in the mid-spanwise plane and (b) in the spanwise-wall-normal plane $x = 8D_o$.

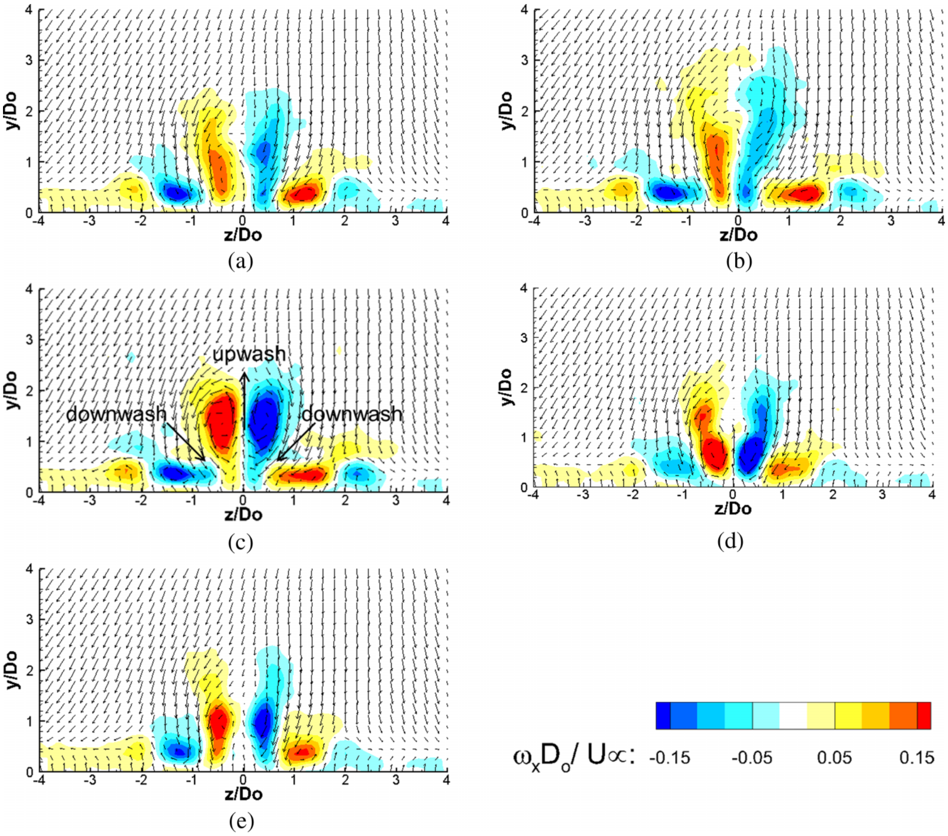

(a) (b) (c) (d) (e)

FIG. 8. Contour of time-averaged streamwise vorticity and velocity vectors in the $x = 8D_o$ plane (a) $\Delta\phi = 0°$, (b) $\Delta\phi = 90°$, (c) $\Delta\phi = 180°$, (d) $\Delta\phi = 270°$, (e) single SJ.

wall at $\Delta\phi = 90°$ as a result of formation of the combined hairpin vortex. However, they are relatively weaker in the time-average sense due to their low occurrence rate and slant hairpin legs. At $\Delta\phi = 270°$, the primary vortices stay lowest and are even lower than those in the single SJ case but are much concentrated and stronger in the time-average sense because of their doubled occurrence rate. For the two cases showing time-averaged partially interacting vortex structures, it is found that the vortices are very strong at $\Delta\phi = 180°$ but weak at $\Delta\phi = 0°$. The reason for the strong vortices at $\Delta\phi = 180°$ is because, as shown in Figs. 5(c) and 6(c), the partially interacting vortex structures are almost parallel to the wall, hence resulting in strong time-averaged vorticity in this spanwise-wall-normal plane. In addition to the vorticity fields, the velocity vectors shown in all the cases reveal that, in the time-average sense, SJs introduce an upwash flow between the two counter-rotating hairpin legs and downwash flows outboard and underneath the legs. These downwash flows can bring outer high-momentum fluid into the near-wall region and hence are very helpful in flow separation control.[28]

As revealed in the above discussions, the boundary layer flow plays an important role in the twin SJ interaction. In return, the twin SJs also influence the boundary layer flow. Fig. 9 shows two overlapping contours: one is the time-averaged wall-normal velocity (contours without colour) and the other is the time-averaged streamwise velocity that is subtracted by the background boundary layer velocity (contours with colour). It is seen that the introduction of SJs into the boundary layer increases the wall-normal velocity downstream of the SJAs. In this aspect, all twin SJs exert much greater influence than the single SJ, as demonstrated by the continuity of the contour lines. Among the four twin SJ cases, the influence of the case at $\Delta\phi = 90°$ most penetrates into the crossflow because of the aforementioned constructive interaction of the two hairpin vortices. From the color contours of streamwise velocities, it is seen that the introduction of SJs produces a slant strip of velocity deficit (in blue) along the trajectories of hairpin heads, as well as a strip of velocity surplus

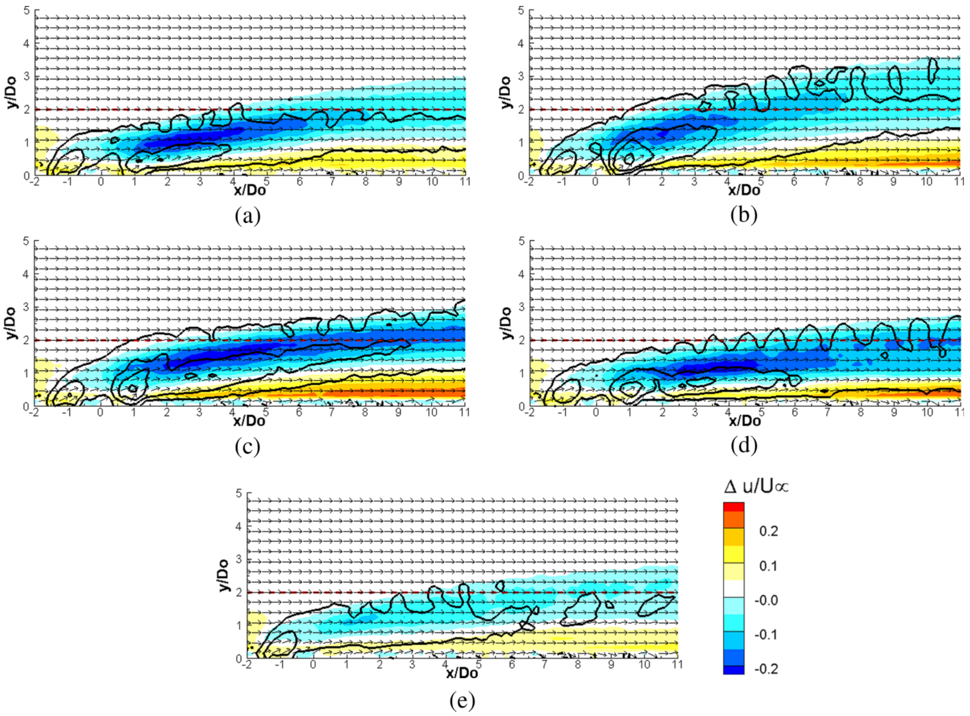

FIG. 9. Contour lines of time-averaged wall-normal velocity (without colour, using the same contour levels as in Fig. 4(b)) superimposed by contours of streamwise velocity difference between SJ influenced flows and the background boundary layer flow (with colour). The vectors are for time-averaged absolute velocities (a) $\Delta\phi = 0°$, (b) $\Delta\phi = 90°$, (c) $\Delta\phi = 180°$, (d) $\Delta\phi = 270°$, (e) single SJ.

(in red) near the wall. The emergence of near-wall velocity surplus well demonstrates the capability of SJs in energizing near-wall flow, which is a favorable feature of flow separation control. It is found that the twin SJs at all $\Delta\phi$ show greater near-wall velocity surplus than the single SJ. Among the four twin SJs cases, it is the case at $\Delta\phi = 180°$ instead of at $\Delta\phi = 270°$ that shows the greatest near-wall velocity surplus. Although it seems not reasonable, the reason can be found in Fig. 8. As shown in Fig. 8(c), the high position of the two counter-rotating vortices makes the downwash flow dominant in the mid-span plane that energizes the near-wall flow, whereas in Fig. 8(d), the low position of the vortex pair causes mainly the upwash flow in the mid-span plane.

B. DMD analysis

DMD analysis is conducted to extract coherent flow structures produced by the in-line twin SJs, so that the dynamics of the present flow system can be seen more clearly. Fig. 10(a) shows the distribution of DMD eigenvalues for the single SJ case, in which each eigenvalue is represented by a circular marker in a space spanned by the real and imaginary parts of the eigenvalue μ_n. All the eigenvalues appear in complex conjugate pairs, as expected due to the convective nature of the boundary layer flow, and their real parts are all negative, indicating the stable nature of this SJ-boundary-layer system. The size of markers is proportional to the DMD mode amplitude b_n (see Eq. (9)), which indicates the spatial coherence of associated dynamic modes, i.e., larger symbols correspond to large-scale structures. It shows that the largest two marker pairs are located at $\mu_i/2\pi = 2$ Hz and 4 Hz, respectively, i.e., the fundamental and second harmonics of the SJ actuation frequency. This confirms the multiple-frequency nature of the present flow system.

The DMD modes corresponding to the largest two marker pairs for the single SJ are plotted in Figs. 10(b) and 10(c). Note the two modes of each pair are exactly the same, and therefore only one from each pair is shown as a representative. Since their dominant frequency coincides with the SJ actuation frequency, the first pair of modes is associated with the convection of hairpin vortices

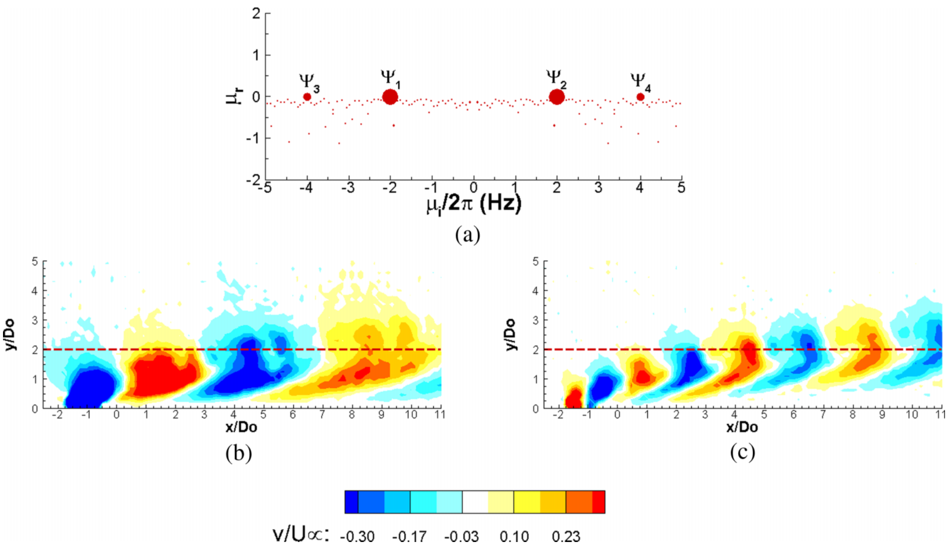

(a)

(b)

(c)

FIG. 10. DMD analysis for the single SJ case: (a) scatters of DMD eigenvalue, and contours of wall-normal velocity of (b) mode Ψ_1 and (c) mode Ψ_3.

induced by the SJ. The second pair of modes, as shown in Fig. 10(c), corresponds to the flow patterns of second harmonic, demonstrating the nonlinearity of the SJ-boundary-layer interaction flow.

As the twin SJs operate at $\Delta\phi = 90°$ and generate combined hairpin vortices, the DMD eigenvalues show a similar distribution to that in the single SJ case, but with significantly increased sizes of the largest two marker pairs as showed in Fig. 11(a). In addition, the coherent structures shown in the first four DMD modes also appear similar to those in the single SJ case, but with obviously increased size and strength. These results confirm the constructive interaction of the twin SJs at this phase difference.

As the twin SJs operate at $\Delta\phi = 270°$ and generate two completely separated hairpin vortices, it is seen from the distribution of DMD eigenvalues shown in Fig. 12(a) that the size of the largest marker pair remains almost unchanged compared to that in the single SJ case, whereas the size of the second largest marker pair increases significantly to a size almost equal to that of the largest marker pair. This change indicates that both the first two DMD mode pairs have almost equal contributions to the dynamics of the flow system. The coherent structures of mode Ψ_1 (shown in Fig. 12(b)) are mainly located near the two SJAs ($x = \pm 1 D_o$), and no coherent structures appear

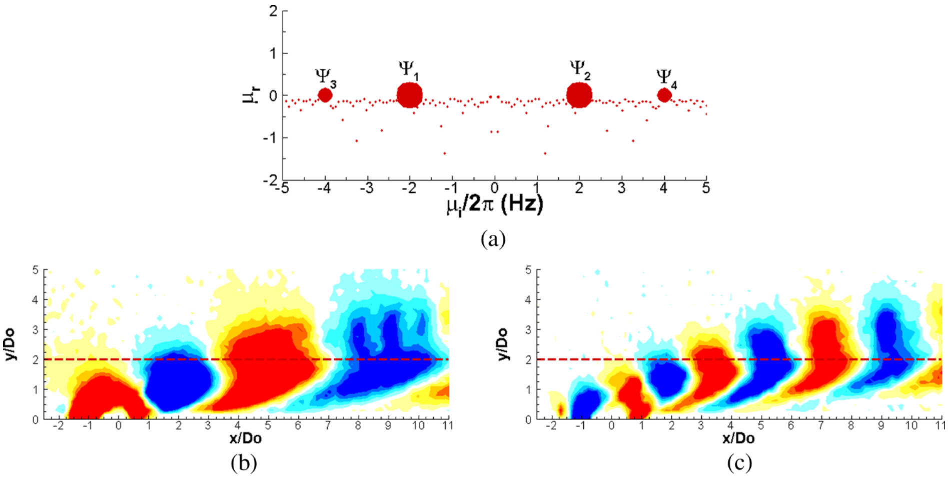

(a)

(b)

(c)

FIG. 11. DMD analysis for the $\Delta\phi = 90°$ case: (a) scatters of DMD eigenvalue, and contours of wall-normal velocity of (b) mode Ψ_1 and (c) mode Ψ_3. Refer to Fig. 10 for the color map.

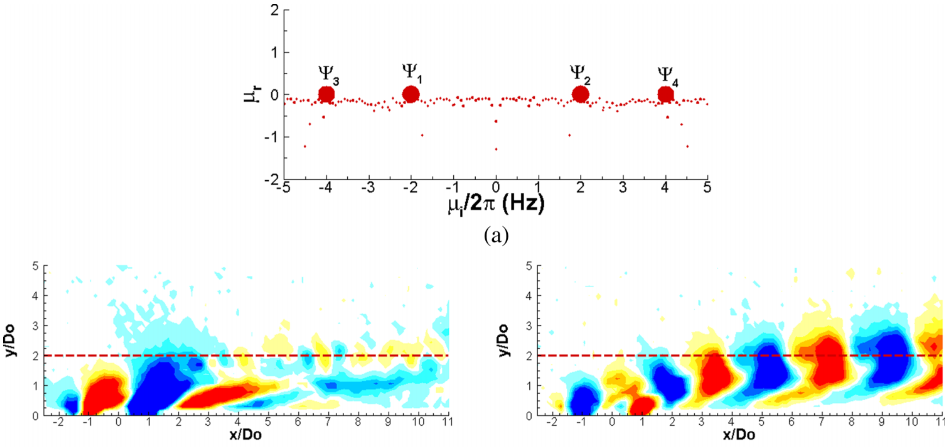

(a)

(b)

(c)

FIG. 12. DMD analysis for the $\Delta\phi = 270°$ case: (a) scatters of DMD eigenvalue, and contours of wall-normal velocity of (b) mode Ψ_1 and (c) mode Ψ_3. Refer to Fig. 10 for the color map.

in the far downstream, indicating that this mode pair captures the flow dynamics associated with the SJ generation that occurs at a frequency of 2 Hz. On the other hand, the coherent structures of mode Ψ_3 (shown in Fig. 12(c)) appear throughout the near-wall region downstream of the SJAs. The frequency they are associated with, i.e., 4 Hz, clearly demonstrates the doubling effect of hairpin vortex appearance rate in this case.

V. CONCLUSIONS

An experimental investigation has been carried out on the vortex dynamics of inline twin SJs operating at various phase differences, i.e., $\Delta\phi = 0°$, 90°, 180°, and 270°, in a flat-plate laminar boundary layer. The results obtained through both dye visualization and PIV measurements were presented to present and analyze the resulting vortex structures. In addition, DMD analysis of the PIV data was conducted to extract representative flow structures. The major findings are summarized as follows:

(1) Depending on the operational phase difference of the twin SJs, three types of vortex structures are identified. At $\Delta\phi = 90°$, the two hairpin vortices interact in a very constructive way in terms of the vortex size, strength, and celerity, forming *a combined vortex*. At $\Delta\phi = 270°$, the two individual hairpin vortices have little interaction, forming *two completely separated hairpin vortices* that behave like doubling the frequency of the single SJ. Due to different levels of disturbance experienced, the hairpin vortex issued from the downstream SJA is generally weaker than its counterpart issued from the upstream SJA. At $\Delta\phi = 0°$ and 180°, the two hairpin vortices produced by the twin SJAs are close enough, with the head of one hairpin vortex coupled with the legs of the other, forming *partially interacting vortex structures*. The trailing vortex behaves quite differently in these two cases: it can sustain its coherence at $\Delta\phi = 0°$ but breaks up into multiple smaller vortex heads at $\Delta\phi = 180°$.

(2) Both spanwise vortex circulation in the mid-span plane and streamwise vortex circulation in a selected spanwise-wall-normal plane ($x = 8D_o$) are calculated from the PIV data at different time instants. The evolutions of spanwise circulation carried by relevant vortex heads reveal that the strength of combined hairpin vortex at $\Delta\phi = 90°$ is the greatest, about 40% larger than that in the single SJ case. At $\Delta\phi = 270°$, the hairpin vortex from the upstream SJA shares very similar circulation evolution process to that in the single SJ case, except that it has a slightly higher peak, whereas the hairpin vortex issued from the downstream SJA shows two significantly lower peaks.

(3) Introduction of SJs into the boundary layer increases the wall-normal velocity in the region downstream of the SJAs. It also produces a slant strip of streamwise velocity deficit along the

trajectories of hairpin heads and a strip of streamwise velocity surplus near the wall. Generally, twin SJs induce larger wall-normal velocity and larger near-wall streamwise velocity surplus compared to the single SJ. Among the four twin SJs cases, it is the case at $\Delta\phi = 180°$ instead of at $\Delta\phi = 270°$ that shows the greatest near-wall velocity surplus.

(4) The DMD analysis confirms the multiple-frequency nature of the present twin SJ flow system. Despite their strength difference, the first two mode pairs in the twin SJ case with $\Delta\phi = 90°$ are similar to those in the single SJ case, both having a dominant first mode pair. For the twin SJ case with $\Delta\phi = 270°$, the second mode pair increases its strength and contributes to the dynamics of the flow system almost equally to the first mode pair.

Through this investigation, a better understanding in the vortex dynamics associated with in-line twin SJs in a laminar boundary layer has been achieved, which provides useful information for future SJ-array applications.

[1] M. Amitay and A. Glezer, “Role of actuation frequency in controlled flow reattachment over a stalled airfoil,” AIAA J. **40**(2), 209 (2002).

[2] M. Amitay, D. R. Smith, V. Kibens, D. E. Parekh, and A. Glezer, “Aerodynamic flow control over an unconventional airfoil using synthetic jet actuators,” AIAA J. **39**(3), 361 (2001).

[3] B. L. Smith and A. Glezer, “The formation and evolution of synthetic jets,” Phys. Fluids **10**(9), 2281 (1998).

[4] S. Zhong, M. Jabbal, H. Tang, L. Garcillan, F. Guo, N. Wood, and C. Warsop, “Towards the design of synthetic-jet actuators for full-scale flight conditions–Part 1: The fluid mechanics of synthetic jet actuators,” Flow, Turbul. Combust. **78**(3-4), 283 (2007).

[5] S. Zhong and S. Zhang, “Further examination of the mechanism of round synthetic jets in delaying turbulent flow separation,” Flow, Turbul. Combust. **91**(1), 177 (2013).

[6] H. Tang, P. Salunkhe, Y. Zheng, J. Du, and Y. Wu, “On the use of synthetic jet actuator arrays for active flow separation control,” Exp. Therm. Fluid Sci. **57**, 1 (2014).

[7] A. Crook and N. Wood, “Measurements and visualisations of synthetic jets,” AIAA Paper 2001-0145, 2001.

[8] M. Ramasamy, J. S. Wilson, and P. B. Martin, “Interaction of synthetic jet with boundary layer using microscopic particle image velocimetry,” J. Aircraft **47**(2), 404 (2010).

[9] S. Zhong, F. Millet, and N. J. Wood, “The behaviour of circular synthetic jets in a laminar boundary layer,” Aeronaut. J. **109**(1100), 461 (2005), see also http://aerosociety.com/News/Publications/Aero-Journal/Online/448/The-behaviour-of-circular-synthetic-jets-in-a-laminar-boundary-layer.

[10] J. Zhou and S. Zhong, “Coherent structures produced by the interaction between synthetic jets and a laminar boundary layer and their surface shear stress patterns,” Comput. Fluids **39**(8), 1296 (2010).

[11] M. Jabbal and S. Zhong, “Particle image velocimetry measurements of the interaction of synthetic jets with a zero-pressure gradient laminar boundary layer,” Phys. Fluids **22**(6), 063603 (2010).

[12] S. Zhang and S. Zhong, “Turbulent flow separation control over a two-dimensional ramp using synthetic jets,” AIAA J. **49**(12), 2637 (2011).

[13] M. Watson, A. J. Jaworski, and N. J. Wood, “Contribution to the understanding of flow interactions between multiple synthetic jets,” AIAA J. **41**(4), 747 (2003).

[14] S. C. Liddle, W. J. Crowther, and N. J. Wood, “Investigation of phase and spacing effects in synthetic jet actuator arrays,” AIAA Paper 2005-107, 2005.

[15] S. C. LIddle and N. J. Wood, “Investigation into clustering of synthetic jet actuators for flow separation control applications,” Aeronaut. J. **109**(1091), 35 (2005), see also http://aerosociety.com/News/Publications/Aero-Journal/Online/487/Investigation-into-Clustering-of-Synthetic-Jet-Actuators.

[16] T. Iai, K. Iwabuchi, M. Motosuke, and S. Honami, “Vortex behavior of in-line synthetic jets in cross flow at low Reynolds number,” AIAA Paper 2010-4412, 2010.

[17] S. Honami and M. Motosuke, “Vortex interaction of in-line synthetic jets injected at difference phase in low Reynolds number cross flow,” AIAA Paper 2012-3243, 2012.

[18] H. Tang and S. Zhong, “Incompressible flow model of synthetic jet actuators,” AIAA J. **44**(4), 908 (2006).

[19] M. Jabbal and S. Zhong, “The near wall effect of synthetic jets in a boundary layer,” Int. J. Heat Fluid Flow **29**(1), 119 (2008).

[20] A. Hjelmfelt and L. Mockros, “Motion of discrete particles in a turbulent fluid,” Appl. Sci. Res. **16**(2), 149 (1966).

[21] R. Mei, “Velocity fidelity of flow tracer particles,” Exp. Fluids **22**(1), 1 (1996).

[22] C. E. Willert and M. Gharib, “Digital particle image velocimetry,” Exp. Fluids **10**(4), 181 (1991).

[23] J. Zhou, R. J. Adrian, S. Balachandar, and T. M. Kendall, “Mechanisms for generating coherent packets of hairpin vortices in channel flow,” J. Fluid Mech. **387**, 353 (1999).

[24] P. J. Schmid, “Dynamic mode decomposition of numerical and experimental data,” J. Fluid Mech. **656**, 5 (2010).

[25] P. J. Schmid, “Application of the dynamic mode decomposition to experimental data,” Exp. Fluids **50**(4), 1123 (2011).

[26] T. Sayadi, P. Schmid, J. W. Nichols, and P. Moin, “Dynamic mode decomposition of controlled H- and K-type transitions,” in *Annual Research Briefs* (Center for Turbulence Research, 2013), p. 189.

[27] X. Wen and H. Tang, “On hairpin vortices induced by circular synthetic jets in laminar and turbulent boundary layers,” Comput. Fluids **95**, 1 (2014).

[28] W. R. Pauley and J. K. Eaton, “Experimental study of the development of longitudinal vortex pairs embedded in a turbulent boundary layer,” AIAA J. **26**(7), 816 (1988).